*energies*

MDPI

*Review*

# Elevating the Practical Application of Sodium-Ion Batteries through Advanced Characterization Studies on Cathodes

**Mengya Li**

Electrification and Energy Infrastructure Division, Oak Ridge National Laboratory, Oak Ridge, TN 37830, USA; lim1@ornl.gov

**Abstract:** Sodium-ion batteries (SIBs) have emerged as promising alternatives to their lithium-ion counterparts due to the abundance of sodium resources and their potential for cost-effective energy storage solutions. The chemistry for SIBs has been investigated since the 1980s, but it went through a slow research and development process. Recently, there has been an acceleration in technology maturation due to a supply chain crisis originating from unequal resource distribution and sustainability and safety concerns regarding lithium-ion batteries. However, the practical application of SIBs has been hindered primarily by challenges related to cathode materials, specifically, surface and structural stabilities in different conditions. Through the integration of advanced techniques such as in situ spectroscopy, operando diffraction, and high-resolution microscopy, a comprehensive understanding of the cathode's dynamic behavior and degradation mechanisms can be achieved. The identified structural modifications, phase transitions, and degradation pathways offer critical insights into the design of robust cathode materials with prolonged cycling stability, fast charging capability, high energy density, great low-temperature performance, and safety. This review underscores the pivotal role of cutting-edge characterization techniques in guiding the development of high-performance sodium-ion batteries, thereby fostering the realization of sustainable and efficient energy storage solutions for diverse technological applications.

**Keywords:** sodium-ion batteries; practical applications; cathodes; advanced characterizations



**Citation:** Li, M. Elevating the Practical Application of Sodium-Ion Batteries through Advanced Characterization Studies on Cathodes. *Energies* **2023**, *16*, 8004. https://doi.org/10.3390/en16248004

Academic Editor: Daniel T. Hallinan Jr.

Received: 27 October 2023
Revised: 21 November 2023
Accepted: 5 December 2023
Published: 11 December 2023



## 1. Introduction

As the critical material prices for lithium-ion batteries (LIBs) continuously rise due to supply chain shortages, it is worthwhile to focus on battery manufacturing beyond lithium-ion batteries. Sodium-ion batteries (SIBs) stand out as one of the great candidates as the electrode materials do not contain cobalt, which is expensive and has humanity issues with the mining process. Instead, earth-abundant transition metal elements such as Cu, Mn, and Fe are often used in sodium-ion cathodes. Sodium-ion battery research emerged in the early 1980s, shortly after Whittingham and Huggins measured the sodium-ion transport properties in sodium β-alumina [1]. Then, after about ten years, sodium-layered oxides and NASICON-type $NaTi_2(PO_4)_3$ were studied as intercalation cathodes [2–5]. Later, due to the successful commercialization of LIBs by Sony [6], there was a pause on sodium-ion battery research for almost 20 years. In 2000, Buiel and Dahn et al. reported a high-capacity hard carbon (HC) anode with a 300 mAh $g^{-1}$ capacity [7–9]. After that, Prussian blue and its analogues (PB&PBAs) were reported as cathodes for SIBs by various institutes around the world [10–13]. Despite the resumed efforts on advancing SIB research, concerns were raised against the existence of molten sodium within batteries, which challenges the safety of battery operation. Regardless, since the late 2010s, an emerging stream of companies and startups started the development and commercialization of SIBs. Currently, there are over 20 companies around the world working on sodium-ion batteries. Although the primary applications of sodium-ion batteries were targeting grid support and electric bikes

or motorcycles, more and more companies have shifted gears towards the development of sodium-ion battery packs for EV applications.

The technology readiness level (TRL) is a metric that reflects the gap between research findings that usually turn out to be publications and technology commercialization. A comprehensive assessment on the battery TRL of various SIB cathodes performed by Baumann et al. indicated that PB derivatives and manganese-based layered oxides are promising candidates considering the cost, raw material criticality, and life cycle carbon footprint [14]. As a groundbreaking event, Contemporary Amperex Technology Co., Limited. (CATL, Ningde, China)'s release on their first-generation SIB in 2021 has profoundly impacted the battery field [15]. With some exciting key parameters reported, CATL's first-generation SIB, which was composed of a Prussian white cathode and an HC anode, can achieve an energy density of 160 Wh $kg^{-1}$ per pack, run for 3000–6000 cycles in its lifetime depending on the scenario, charge to an 80% state-of-charge (SOC) in 15 min, and exhibit a 90% capacity retention at −20 °C. At the same time, it is worthwhile to note that other SIB companies such as Tiamat Energy (Amiens, France), Faradion Ltd. (Sheffield, UK), Natron Energy (Santa Clara, CA, USA), HiNa Battery Technology (Liyang, China), etc., also demonstrated exceptional battery performances that are comparable with lithium-ion phosphate (LFP)-based LIBs. For example, Tiamat Energy commercialized 18,650 SIBs with the $Na_3V_2(PO_4)_2F_3$ cathode against an HC anode and demonstrated more than 5000 cycles with an over 80% capacity retention with the additional claim of a fast charging capability in 5 min [16]. HiNa Battery Technology claimed that their SIBs with a $Na_xCu_yFe_zMn_{1-y-z}O_2$ cathode against soft carbon can achieve an energy density of more than 145 Wh $kg^{-1}$ at the cell level, a working temperature between −40 and 80 °C, and more than 4500 cycles with an 83% capacity retention at 2C/2C [17]. Although the industrial development for SIBs has been skyrocketing, there are still a lot of fundamental science questions remaining to be solved in the research field. Natrium Energy has successfully launched SIBs with a $Na_xNi_{1/3}Fe_{1/3}Mn_{1/3}O_2$ cathode against an HC anode, with a projected production of 80,000 mt of cathode materials in the next 3–5 years [18].

Advanced characterization has been adopted and continuously upgraded to investigate the fundamental chemistry and physics within the battery components, especially on cathode materials [19–21]. However, advanced characterization often requires the utilization of world-class facilities such as neutron and synchrotron beamlines and carefully designed experiments with specific experimental setups. The commonly used characterization techniques, such as scanning electron microscopy (SEM) and X-ray diffraction (XRD), as well as electrochemical testing such as galvanostatic charge/discharge and electrochemical impedance spectroscopy (EIS) still serve as important items on the to-do list for validating materials' morphology, phase properties, and electrochemical performances. Meanwhile, understanding the structural evolution, redox chemistry, kinetics at the surface, interface and bulk, and failure mechanism is crucial for optimizing existing SIB systems and exploring novel materials [22–31]. Advanced characterization in spectroscopic, microscopic, and scattering techniques often provides insights that will expedite the scientific development of batteries in shaping the choice of chemistry, guiding the material engineering, understanding and regulating the interfacial properties, deep diving into the electrode/cell failure mechanism, and validating the cell design. All of the above efforts can parallelly pair with battery manufacturing and testing in academia and industry to further accelerate the commercialization of SIBs.

In this review, we aim to elucidate the implications of state-of-the-art advanced characterization findings on meeting the current parameters and commercial objectives for SIBs. A comprehensive analysis of these advanced characterization results serves as a critical guide for optimizing the performance, enhancing stability, and achieving the requisite energy density for the practical deployment of SIBs on a commercial scale targeting electric vehicles and other applications.

## 2. Metrics That Matter for Practical Sodium-Ion Batteries

For SIBs, HCs have garnered significant attention as promising anode materials, owing to their ability to facilitate the intercalation of sodium ions within pseudo-graphitic domains and their reversible adsorption in surface edges, defects, and nanopores. Derived easily from various types of cost-effective biomasses through high-temperature annealing in an oxygen-free environment, HCs can often achieve reversible capacities of more than 300 mAh $g^{-1}$ with stable cycling demonstrated over thousands of cycles. As a result, the limiting factor in the overall electrochemical performance of the full cell for SIBs often resides in the characteristics of the cathode. The inherent properties of different cathodes will have impacts on the overall cost, energy density, cycle life, low-temperature performance, fast charging capabilities, and safety of SIBs.

One of the key aspects for SIB technology is the low cost of the battery components, especially cathodes, due to there being no engagement of critical materials such as cobalt and lithium in comparison with current LIB technology. Unlike lithium, which is relatively scarce and often extracted through complex mining processes, sodium is abundantly present in various natural sources such as seawater and salt deposits. The ability of using aluminum foil as a current collector for both the anodes and cathodes of SIBs without significant concerns about corrosion further contributes to the overall cost reduction in battery production. Despite the promising cost-reducing factors, doubts persist regarding whether the actual cost of SIBs will be lower than that of LIBs, particularly from an electric vehicle perspective. Li et al. performed a cost analysis of SIBs using a $Na_{0.67}Fe_{0.5}Mn_{0.5}O_2$ cathode and a hard carbon anode and compared it with LIBs using a $Li_{1.05}(Ni_{0.6}Mn_{0.2}Co_{0.2})_{0.95}O_2$ (NMC622) cathode and a graphite anode using a 53 kWh pack with a BatPac model developed by Argonne National Laboratory [32]. The results showed that the cost of the SIB pack (USD 5925) is not substantially lower than the LIB pack (USD 5875), but there are promises to further lower the cost by optimizing the materials and increasing the energy density of SIBs [33]. Nonetheless, considering geopolitical issues and the supply chain shortage, SIBs can have substantial cost competitiveness compared to LIBs [34].

Energy density improvement is crucial for SIBs in EV applications, given that SIBs have often been viewed as a subsidiary technology to LIBs owing to their comparatively lower energy density values. When manufacturing batteries for EV applications, investors and consumers express concerns about the car's range, which is directly linked to the energy density of the battery pack. The energy density values reported in literature are often based on material chemistry, mostly in half cells, rather than the cell level numbers for full-cell configurations. Given the constraints in battery labs and facilities at universities or other academic institutions, it is understandable that the manufacturing of actual battery packs poses a significant challenge. Thus, more reliable estimations should be performed when reporting energy density values based on a new chemistry or new material. The incorporation of at least the masses of both electrodes (cathode and HC anode) in a full-cell configuration is essential. CATL's first-generation SIBs based on Prussian white chemistry claim to achieve a 160 Wh $kg^{-1}$ energy density, with the next generation expected to achieve a 200 Wh $kg^{-1}$ energy density. It is worth noting that Tiamat commercialized 18,650 cells with $Na_3V_2(PO_4)_2F_3$; however, the actual energy density at the cell level is only 100–120 Wh $kg^{-1}$. The Singapore-based SgNaPlus claimed that their NVPF-based battery pack reaches only 65–70 Wh $kg^{-1}$. While practical LIBs based on LFP technology can reach a 160–180 Wh $kg^{-1}$ energy density at the cell level, there is still a long way to go to improve the energy density of NVPF-based SIBs.

The cycle life has remained as a key aspect for SIBs regarding cell durability. Since $Na^+$ (ionic radius: 1.02 Å) is a bigger ion than $Li^+$ (0.76 Å), continuous intercalation/deintercalation into the cathode and anode materials often end up with more severe structural distortion. The cycling stability of each cathode/anode material is dictated by the structural stability, electrolyte stability, cathode- or anode-electrolyte interphase (CEI and SEI) properties, operating voltage range, and discharging current. Improving the reversible structural evolution of the cathode material is crucial for extending the cycle lives of SIBs. Introducing doping elements

such as transition metals can effectively modify the crystal structure, enhancing the stability and structural integrity of the cathode material during repeated cycling [35–37]. Simultaneously, surface stabilization, carried out by coating the cathode with protective layers, can mitigate the detrimental effects of side reactions at the interface and electrolyte degradation, thereby minimizing capacity fading and preserving the structural integrity of the cathode material over prolonged cycling [38–40]. The cycling stability not only depends on the cell chemistry and material structure, but it is also affected by the testing protocols such as the current density and depth-of-discharge (DOD). While there is not a standard performance benchmarking manual for SIBs yet, it is worth noticing that companies that have commercialized their SIB technologies have been shooting for 3000–5000 cycles of their batteries with a capacity retention close to 80% (see Figure 1a,b). Natron Energy has commercialized their SIBs based on a PB cathode with zero strain during charging and discharging, thus making them capable of achieving over 50,000 cycles [41].

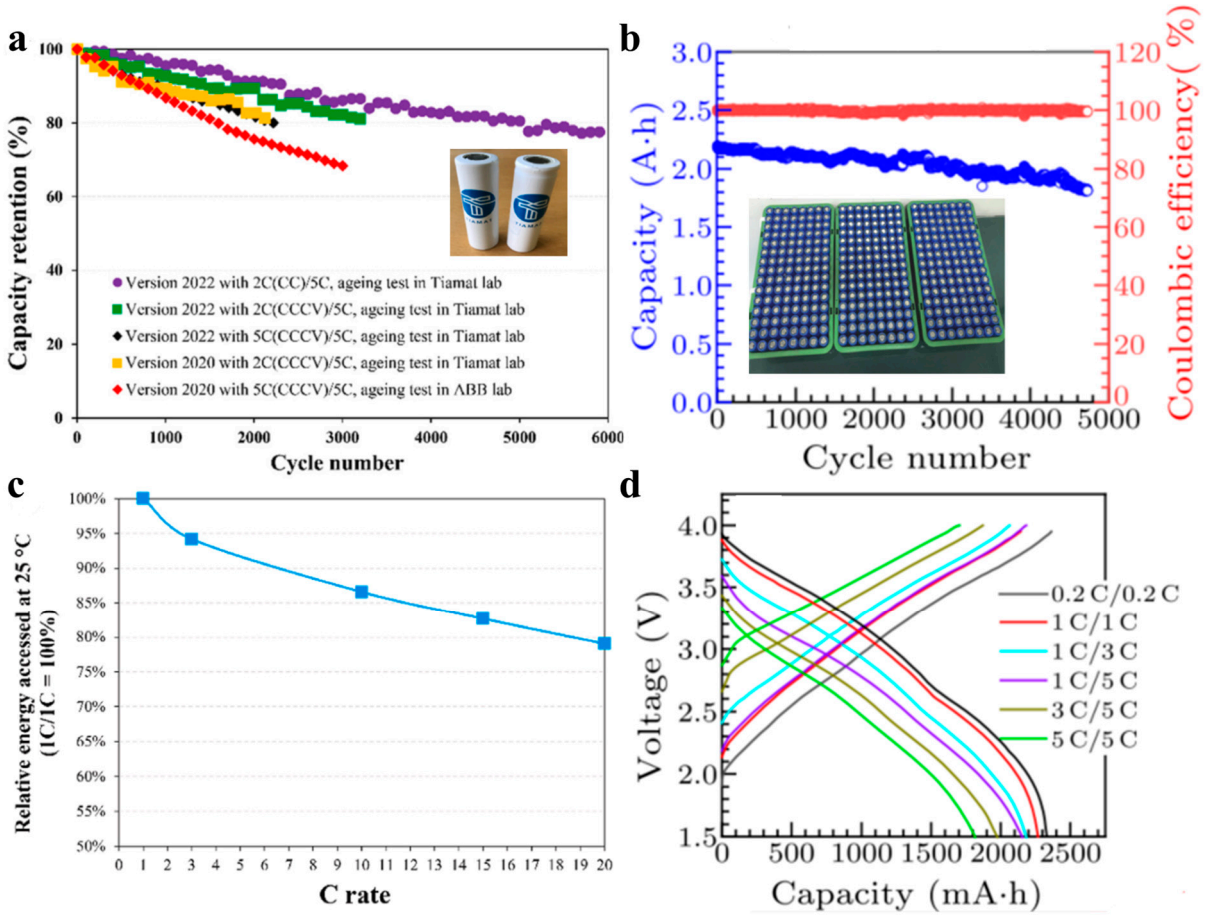


**Figure 1.** (**a**) Tiamat Energy's cylindrical 18650-type SIBs cycle lives, measured at 25 °C and 100% DOD in 2023 [16]. (**b**) HiNa Battery Technology's high-power cylindrical 26650-type SIBs with cycling performance at 2 C/2 C rate in 2021 [17]. (**c**) Comparison of relative energy at different discharge C rates for Tiamat Energy's cylindrical 18650-type SIBs. (**d**) Charge–discharge curves at different rates of HiNa Battery Technology's cylindrical 26650-type SIBs.

Power capability is also crucial in the sense of fast charging. One of the biggest concerns centered around EVs is always on the length of charging. The benefits of EV include environmental friendliness. As more and more consumers become aware of the positive environmental impact that EVs provide, other matters regarding the price, range, and charging time still need to be considered before making a decision to shift from conventional gasoline cars to EVs. Although the time of adding gas to a conventional car depends on the gas tank capacity, with sedans usually falling into ranges between 12 and

16 gallons, and SUVs falling between 18 and 34 gallons, the average gas tank filling time should be no more than 10 min, assuming that the tank started very low or the pump is running slowly. While current electric vehicles available on the market, powered by LIBs, require at least 15 minutes to complete a 20% to 80% state of charge (SOC) cycle, it is crucial to explore SIBs equipped with electrodes and electrolytes capable of achieving charging times equal to or shorter than those of the existing LIBs. The limitation with LIBs regarding fast charging is primarily due to the graphite anode. When the charging rate exceeds the intercalation rate of $Li^+$ into graphite anodes, it can frequently result in lithium plating on the surface of the graphite anode, thereby giving rise to safety concerns. For SIBs, the $Na^+$ storage mechanism in HC anodes is not an intercalation-only mechanism anymore. Because of the functional surface and porous structure of the graphitic nanodomains within HC anodes, the charge transfer properties are generally enhanced in comparison to $Li^+$ in graphite. Therefore, it became important to search for good cathode and electrolyte candidates that can enable fast $Na^+$ ion transporting properties to realize a practical SIB with a fast charging capability (see Figure 1c,d). It is worth noting that Tiamat has demonstrated excellent power capability in their 18,650 SIBs based on NVPF/HC chemistry, with more than 90% of capacity accessible at a 20 C discharge [16].

Low-temperature performance has been considered as a key metric of batteries for EV applications. It is known that the range of currently commercialized EVs in cold weather drops drastically due to the much-degraded performance of LIBs. SIBs, on the other hand, can exhibit great low-temperature performance by optimizing the anode, cathode, and electrolyte. The development of cathode materials for SIBs at low temperatures involves addressing challenges related to the specific capacity, diffusion rates, and electronic conductivity. Strategies such as nanostructuring, synergistic effects of transition metal ions by doping, and 3D composite construction have shown promise in enhancing the electrochemical performances of these materials. Layered transition metal oxide cathodes can demonstrate a reversible capacity of 142 mAh $g^{-1}$ at −20 °C with a 68.2% capacity retention after 100 cycles at 0.5 C (1 C = 170 mA $g^{-1}$) [42]. A sodium-rich PB-carbon nanotube composite cathode can deliver 114 and 88.4 mAh $g^{-1}$ at 2.4 C (1 C = mA $g^{-1}$) with capacity retentions of 81% and 86% after 1000 cycles at 0 °C and −20 °C, respectively [43]. Polyanion cathodes with transition metal doping can achieve a reversible capacity of 79.9 mAh $g^{-1}$ at −25 °C and a capacity retention of >90% after 400 cycles at 0.5 C (1 C = 128 mA $g^{-1}$) [44].

Apart from the above aspects, safety is also a key metric to consider for successful research on technology transfer. From storing and transportation perspectives, LIBs can experience severe cycle life reduction and even potential fires or explosions when discharged below their rated 0% state of charge (SOC), and they also cannot exceed a 30% SOC during shipping in order to maintain thermal stability. On the contrary, SIBs can be discharged to 0 V, primarily due to the use of aluminum current collectors for both the cathode and anode. The capability of Na-ion cells to be stored and transported at 0 volts provides logistical flexibility for manufacturers, enabling safer handling during installation and reducing the risks associated with energy storage. Natron Energy has performed comprehensive safety tests on their SIBs including nail penetration, a crush test, high-speed projectile test, and cut test, with all of the results demonstrating a safer pouch cell in comparison with a NMC532-based LIB [45].

## 3. Guidance from Cutting-Edge Advanced Characterization Results

Advanced characterization techniques that require specific facilities and carefully designed experimental setups play a crucial role in understanding the fundamental science within the batteries and battery components and provide guidance on the choice of chemistry regarding different applications. Neutrons are sensitive towards light elements, and they are commonly employed in charactering battery components [46]. Neutron scattering can provide fine structural details, which are crucial for assessing factors such as the cycle life and performance at varying temperatures. Similarly, a neutron pair distribution function (PDF) analysis augments this understanding by delving deeper into the local structures,

influencing the safety evaluations and performance predictions, especially under diverse operational conditions [35,47–50]. Synchrotron characterizations, on the other hand, can provide information on the local structure as well, especially when heavy elements are involved. In situ synchrotron powder X-ray diffraction can be used to characterize the structural evolution of sodium cathodes upon charging and discharging [26,51,52]. The validation of reversible phase changes and minimum volume expansion/contraction serves as an important step towards advancing the material's TRL. Furthermore, the low-temperature performance of SIBs relies on the efficiency of the charge-transfer process, a factor that is closely linked to the structural and interfacial properties of materials. These aspects can be effectively resolved through advanced characterization techniques like synchrotron XRD and high-resolution X-ray photoelectron spectroscopy (XPS) with depth profiling results. Synchrotron X-ray absorption near-edge structure (XANES) and extended X-ray absorption fine-structure (EXAFS) results offer valuable insights into the redox mechanisms governing the oxidation states of elements within cathode materials and the local structural changes of the cathode materials [26,53,54]. Resonant inelastic X-ray scattering (RIXS), with its enhanced sensitivity to chemical states and capacity to distinguish intrinsic oxidized oxygen in the lattice, provides crucial insights into bulk oxygen redox that conventional X-ray absorption spectroscopy might miss [55–57]. This is particularly relevant for addressing challenges associated with the surface effect in anionic redox couple exploitation and for elucidating the complicated interplay between cathode and anode reactions, contributing significantly to the development of practical high-voltage and high-capacity SIBs.

Apart from synchrotron characterization techniques, the use of an electron beam under a cryogenic atmosphere can also become a useful strategy in understanding the cathode–electrolyte interphase (CEI) formed on the surface of cathodes and the stability of the CEI towards the overall SIB electrochemical performance. While the CEI is not only dependent on cathode materials but also on the electrolyte choice, surface coating has remained an effective strategy in improving the stability of the CEI apart from the exploration of different electrolytes. Advanced imaging such as scanning transmission electron microscopy–electron energy loss spectroscopy (STEM-EELS) mapping by cryo-EM or atomic force microscopy (AFM) coupled with analytic techniques such as time-of-flight secondary ion mass spectrometry (ToF-SIMS) can provide more detailed information on the CEI composition and evolution. AFM ToF-SIMS offers the capability of achieving high lateral resolution, reaching as low as 50 nm, and wide fields of view, extending up to several centimeters. Additionally, it enables high mass resolution ($m/\Delta m > 30{,}000$ FWHM), facilitating the differentiation of ion species that share similar masses [58]. When coupling AFM ToF-SIMS with XPS depth profiling, a detailed picture of the surface layer composition can be revealed. Moreover, the analysis of the AFM ToF-SIMS depth profiling results can enable reconstructed 2D or 3D images to extract information regarding the distribution of organic/inorganic components in the bulk. The abovementioned techniques correlate with metrics such as energy density and power capability, enabling a comprehensive understanding of material behaviors that are crucial for optimizing battery performance in terms of the energy storage, power delivery, and longevity.

### *3.1. Sodium-Layered Oxide*

For a sodium-layered oxide cathode, Cedar et al. reported in 2011 that monoclinic $\alpha$-$NaMnO_2$ has poor structural stability due to the Jahn–Teller active $Mn^{3+}$ ion, even though the initial reversible capacity can reach 185 mAh/g [59]. Komaba et al. reported in 2012 that the cycling stability of $\alpha$-$NaFeO_2$ significantly drops, which is associated with the irreversible structural change when more than 0.5 mole of $Na^+$ is removed during charging [60]. Later on, enormous research efforts have been focused on doping strategies by incorporating two, three, or even more transition metal elements to obtain stable lattice structure and suppress the reactivity of the Jahn–Teller active $Mn^{3+}$. The results showed that single- or multi-element doping by Li [61], B [62], Mg [63], Al [64], Ti [65], Fe [66], Co [67], Ni [68], Cu [69], or Zn [52] can improve the reversible capac-

ity and cycling retention of $NaMnO_2$. Among these materials, the primary structure is often either $P_2$ or $O_3$ based on the atomic arrangement. P2-type materials (where the Na ion sits in the prismatic site) often have smaller energy density values because of a Na-deficient composition, but they can demonstrate stable cycling performances. The synchrotron-based in situ high-energy X-ray diffraction (HEXRD) results showed that the P2-type $Na_{0.66}Ni_{0.33}Mn_{0.67}O_2$ undergoes a smaller degree of gliding between transition metal layers and smaller changes in the interlayer spacing during cycling, but a higher irreversible P2-P'2 phase change. With Zn doping, $Na_{0.66}Ni_{0.26}Zn_{0.07}Mn_{0.67}O_2$ exhibits a more reversible P2-O2 phase transition through a glide of the transition metal layer [70]. Song et al. reported a novel P3-type $Na_{2/3}Mg_{1/3}Mn_{2/3}O_2$ material with exceptional initial reversible capacity exceeding 220 mAh $g^{-1}$ when charging up to 4.65 V. XANES, and the EXAFS results suggested a partial $Mn^{3+}/Mn^{4+}$ cationic redox with a reversible migration of $Mg^{2+}$ between the transition metal octahedral sites and the interlayer tetrahedral sites with an additional hypothesis of a reversible $O^{2-}/O^{-}$ anionic lattice oxygen redox (Figure 2a,b) [71]. Neutron diffraction and PDF characterizations on charged and discharged P3-type $Na_{0.6}[Li_{0.2}Mn_{0.8}]O_2$ revealed the evolution of the O-O distance within the $Mn(Li)O_6$ octahedra and concluded the existence of rigid lattice oxygen, which can effectively stabilize the reduced oxygen ions and further enable reversible oxygen anion redox (Figure 2c) [72]. In contrast, O3-type materials (where the Na ion sits in the octahedral site) can often provide a higher energy density, but struggle with long-term cycling stability and higher degrees of structural changes. Jin et al. demonstrated the full-cell performance of an O3-type $NaCu_{1/9}Ni_{2/9}Fe_{1/3}Mn_{1/3}O_2$ with a 97.5 mAh $g^{-1}$ reversible capacity and a capacity retention of 82.5% after 200 cycles. The cryo-transmission electron microscopy results showed that an ultrathin (3 nm) and robust CEI formed on the cathode surface in contact with a localized high-concentration electrolyte (LHCE) can block transition metal dissolutions and minimize the surface reconstructions of the O3-type $NaCu_{1/9}Ni_{2/9}Fe_{1/3}Mn_{1/3}O_2$ cathode [73]. Wang et al. demonstrated the scalable synthesis of an O3-type $Na_xNi_{1/3}Fe_{1/3}Mn_{1/3}O_2$ and half-cell capacities of 124 mAh $g^{-1}$ (55 °C) and 72 mAh $g^{-1}$ (−20 °C). In addition, a 1 Ah SIB full-cell pack cycled between 1.5 and 3.8 V at room temperature exhibited a 73% capacity retention after 500 cycles at a 1C rate (1C = 130 mAh $g^{-1}$) [74]. As a follow-up study, Xie et al. validated that the origin of the stable electrochemical performance of $NaNi_{1/3}Fe_{1/3}Mn_{1/3}O_2$ comes from the in situ formation of a strained O/P composite by using in situ HEXRD and both operando Bragg coherent diffraction (BCXD) and coherent multicrystal diffraction (CMCD) (Figure 2d–f) [75]. Xie et al. further combined HEXRD with accelerated rate calorimetry (ARC) and confirmed great thermal and chemical stability of the O3-type $NaNi_{1/3}Fe_{1/3}Mn_{1/3}O_2$ [76]. For storage purposes, the O3-type layered oxides often struggle with air stability. Yao et al. demonstrated that the Cu/Ti co-doping of the O3-type $NaNi_{0.5}Mn_{0.5}O_2$ can effectively increase the material air stability with ex situ synchrotron XANES results [77].

### *3.2. Prussian Blue and Its Analogues*

Prussian blue (PB) is a low-cost synthetic pigment that was first developed by accident in 1704. While its impact has greatly benefited the artistic field in the 19th century, it was not until the 2010s when researchers found possibilities of using PBs and Prussian blue analogues (PBAs) as cathode materials for SIBs [10]. Unlike layered oxides, the structures of PBs and PBAs contain rigid open frameworks and large interstitial sites that can enable rapid $Na^+$ diffusion with minimum structural deterioration [78,79]. For applications towards practical SIBs, it is preferrable to have a sodium-rich and low-vacancy phase so that the Na inventory will not lose much in a full cell against the HC anode, and there can be more $Na^+$ active redox sites [80–82]. Adak et al. screened the Cr, Mn, Fe, Co, Ni, Cu, and K-edge XANES spectra of a series of PBAs to obtain the oxidation states of each TM element and provided insights on the correlation between thermal expansion observed in these materials and the oxidation states of the TM ions [83]. Reversible phase transitions between rhombohedral, cubic, and tetragonal phases was revealed from in situ synchrotron

XRD results for $Na_{1.73}Fe[Fe(CN)_6]\cdot 3.8H_2O$ by Wang et al. [23]. Low-cost Mn-based PBAs are demonstrated with excellent high voltage performances, which have driven advanced characterization studies towards understanding the redox mechanism. Sottmann et al. performed operando synchrotron XAS on $Na_{1.32}Mn[Fe(CN)_6]_{0.83}\cdot zH_2O$ and concluded a redox mechanism based on the formation of three phases along with an $Fe^{2+}/^{3+}$ and $Mn^{2+}/^{3+}$ redox [54]. Xie et al. attributed the long lifespan of a Mn-, Co-, and Ni-co-doped PBA composite with eliminated parasitical coordinated water to a relieved lattice volume and stress changes during the insertion and extraction of $Na^+$ from ex situ XANES and EXAFS results [84]. With the in situ synchrotron XRD and ex situ soft XAS results, Pasta et al. found that the crystal structure of manganese/cobalt hexacyanoferrate can be maintained if cycling the C-coordinated Fe, with outstanding kinetics and cycle life. The N-coordinated Co and Mn ions exhibit a slower kinetic regime due to structural distortions, but they still contribute significantly towards the high specific capacity (Figure 3a–c) [85]. Ni-based PBAs have raised interest due to the zero-strain properties during $Na^+$ insertion/extraction [86]. Gebert et al. showed that a continuous and coherent lattice across the interface of the Mn-rich inner and Ni-rich outer layer exists for the NiPB-stabilized MnPB from cryo-high-resolution transmission electron microscopy (HRTEM) with FFT (Figure 3d–h) [87]. It is also worth noting that the scalable production of sodium-rich PBs and PBAs is challenging due to the difficulty remaining with precisely controlling the coordinated water content in each synthesis batch. Despite the challenges, Wang et al. demonstrated the feasibility of a low-cost, sodium-rich, dehydrated, and air-stable Prussian white cathode. By correlating the high and low voltage plateaus towards a redox reaction on the $FeN_6$ octahedra and the $FeC_6$ centers through soft X-ray absorption spectroscopy (sXAS) results, a full-cell capacity of 119.4 mAh $g^{-1}$ can be realized with a 94% capacity retention after 50 cycles (Figure 3i) [88]. Shortly after 6 years, CATL's first-generation SIBs based on the same Prussian white HC configuration were released.

### *3.3. Phosphates (or Polyanions)*

Sodium vanadium phosphates—$Na_3V_2(PO_4)_3$—have also drawn a lot of interest in the SIB research field due to its Na super-ionic conducting (NASICON)-like structure that provides a high-rate capability and high energy density with a higher operating voltage [89,90]. Recent advancements in the characterization of these cathodes have provided valuable insights into their performance. For instance, HRTEM can reveal the nanoscale architecture of sodium polyanion cathodes, highlighting the presence of well-defined polyanion frameworks that facilitate efficient sodium ion diffusion [91]. Furthermore, spectroscopic techniques such as XAS have played crucial roles in elucidating the redox mechanism, local structural changes, and degradation pathways [92]. Qin et al. performed XPS, AFM ToF-SIMS, and operando isothermal microcalorimetry (IMC) and confirmed that an effective polymer–inorganic CEI can form between ether-based electrolyte (1 M $NaPF_6$ in diglyme) and $Na_3V_2(PO_4)_3$ electrodes, which enables stable cycling and fast charge transfer (Figure 4) [93]. To improve the poor conductivity of polyanion materials, Shin et al. found a stable interface between $Na_3V_2(PO_4)_3$ and a reduced graphene oxide layer from the STEM-EELS mapping results, which validated the superior cycling stability of this composite cathode with a capacity retention of 91% after 10,000 cycles at 50 C [94]. Fluorine doping has been found capable of further increasing the operating voltage and the stability of the $Na_3V_2(PO_4)_3$ electrodes [95,96]. Broux et al. confirmed the disproportionation of two $V^{IV}$ into $V^{III}$ and $V^{V}$ in the $V_2(PO_4)_2F_3$ bioctahedra upon sodium extraction from NVPF electrodes to be the primary redox mechanism [97]. Iarchuk et al. further validated this $V^{IV}$ disproportionation in $Na_{3+x}V_{2-y}Mn_y(PO_4)_2F_3$ from core-loss EELS spectra [98]. The experimental results validated that the extraction of two $Na^+$ ions of $Na_3V_2(PO_4)_2F_3$ (NVPF) at voltage plateaus of 3.7 and 4.2 V vs. $Na/Na^+$ can potentially enable an energy density of 507 Wh $kg^{-1}$ at the material level, which is comparable with the $LiFePO_4$ (LFP) technology [99]. Fe-based sodium polyanion cathodes have also drawn attention due to the $Fe^{3+}/Fe^{2+}$ and $Fe^{4+}/Fe^{3+}$ electrochemically active redox pairs. Liu et al. reported a highly

reversible $Na_{3.32}Fe_{2.11}Ca_{0.23}(P_2O_7)_2$ cathode with an 81.7% capacity retention at 1 C due to the single-phase solid solution reaction, which was confirmed by operando synchrotron-based XRD and in situ XANES results [100]. Oyama et al. demonstrated reversible valence state changes in Fe from ex situ XANES results, and proposed an irreversible rearrangement reaction of $Na_{2+2x}Fe_{2-x}(SO_4)_3$, resulting from Fe migration to Na site [101]. While the operating voltage of sodium polyanion cathodes typically exceeds that of sodium-layered oxide or Prussian blue cathodes, their practical energy density remains relatively low due to their inherent poor conductivity. Incorporating functional carbon materials as solutions can be imperative, yet it must be executed judiciously to avoid significant sacrifices in the energy density.

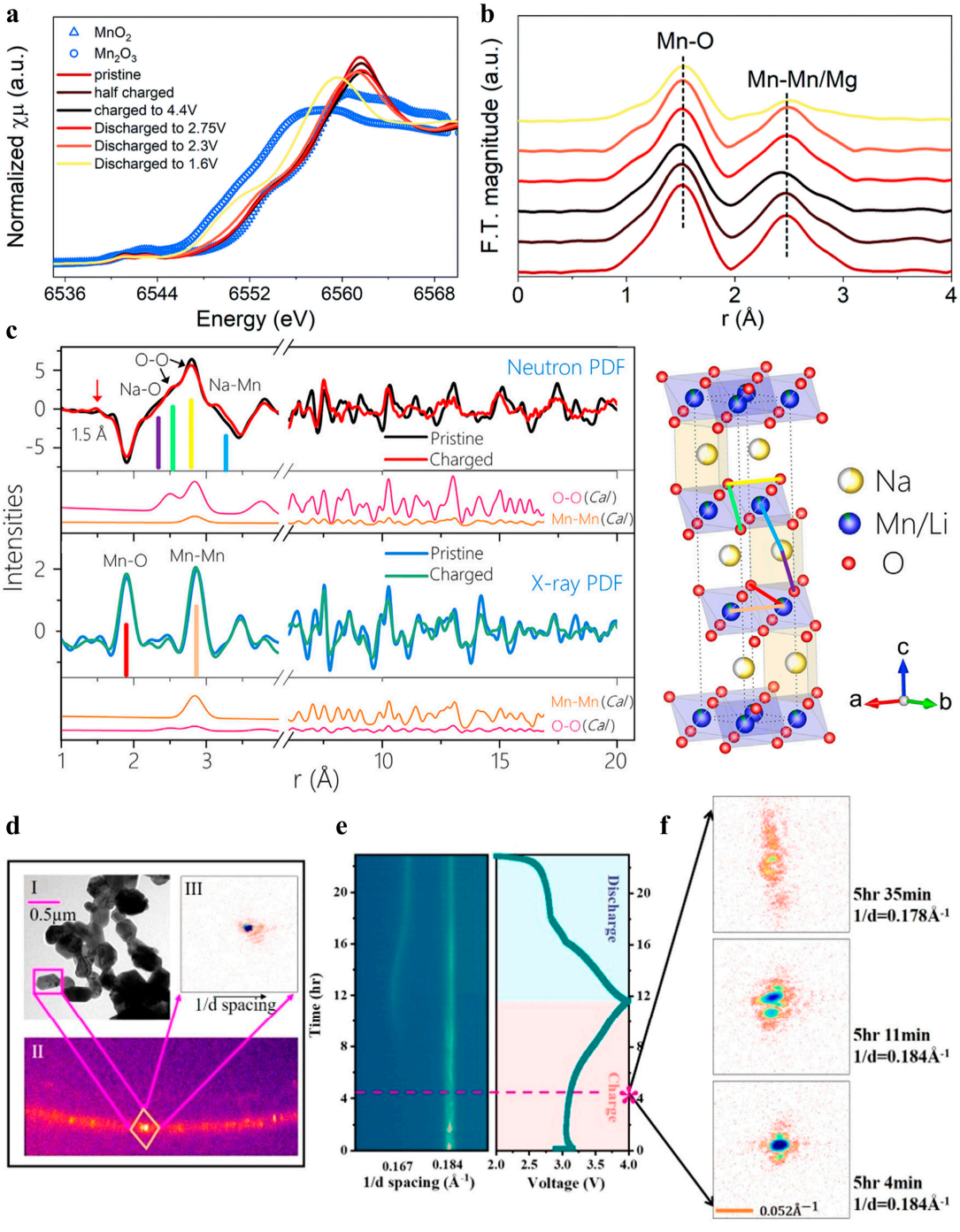


**Figure 2.** (**a**) X-ray absorption near edge structure (XANES) of the P3-type $Na_{2/3}Mg_{1/3}Mn_{2/3}O_2$ at various states of charge/discharge with references of $Mn_2O_3$ and $MnO_2$ shown. (**b**) Fourier-transformed

EXAFS of P3-type $Na_{2/3}Mg_{1/3}Mn_{2/3}O_2$ at various states of charge. The color code in all panels is the same as that in (**a**) [71]. (**c**) Comparison of X-ray and neutron PDF of $Na_{0.6}[Li_{0.2}Mn_{0.8}]O_2$ collected at pristine and charged state (4.5 V). The representative peaks corresponding to bonds such as the first coordinating O-O, Mn-O, and Mn-Mn bonds are labeled [72]. (**d**) Experimental schematic of BCXD (Bragg coherent X-ray diffraction): (I) TEM image of partial single crystals from the sample; (II) CMCD (coherent multicrystal diffraction; signal scattered by partial single crystals from $NaNi_{1/3}Fe_{1/3}Mn_{1/3}O_2$ particle, satisfying the Bragg condition recorded at the detector; yellow diamond (Bragg spot of one of the single crystals); (III) BCDI (Bragg coherent diffractive imaging)—Bragg spot of one of the single crystals recorded at the Medipix detector. (**e**) CMCD (coherent multicrystal diffraction; left) for the (003) peak along with charge-and-discharge curve of $NaNi_{1/3}Fe_{1/3}Mn_{1/3}O_2$ materials (right; initial multicrystal diffraction). (**f**) BCDI (Bragg coherent diffractive imaging) during the phase transition process (in response to the phase transition that happened at 3.2 V in panel (**b**)) [75].

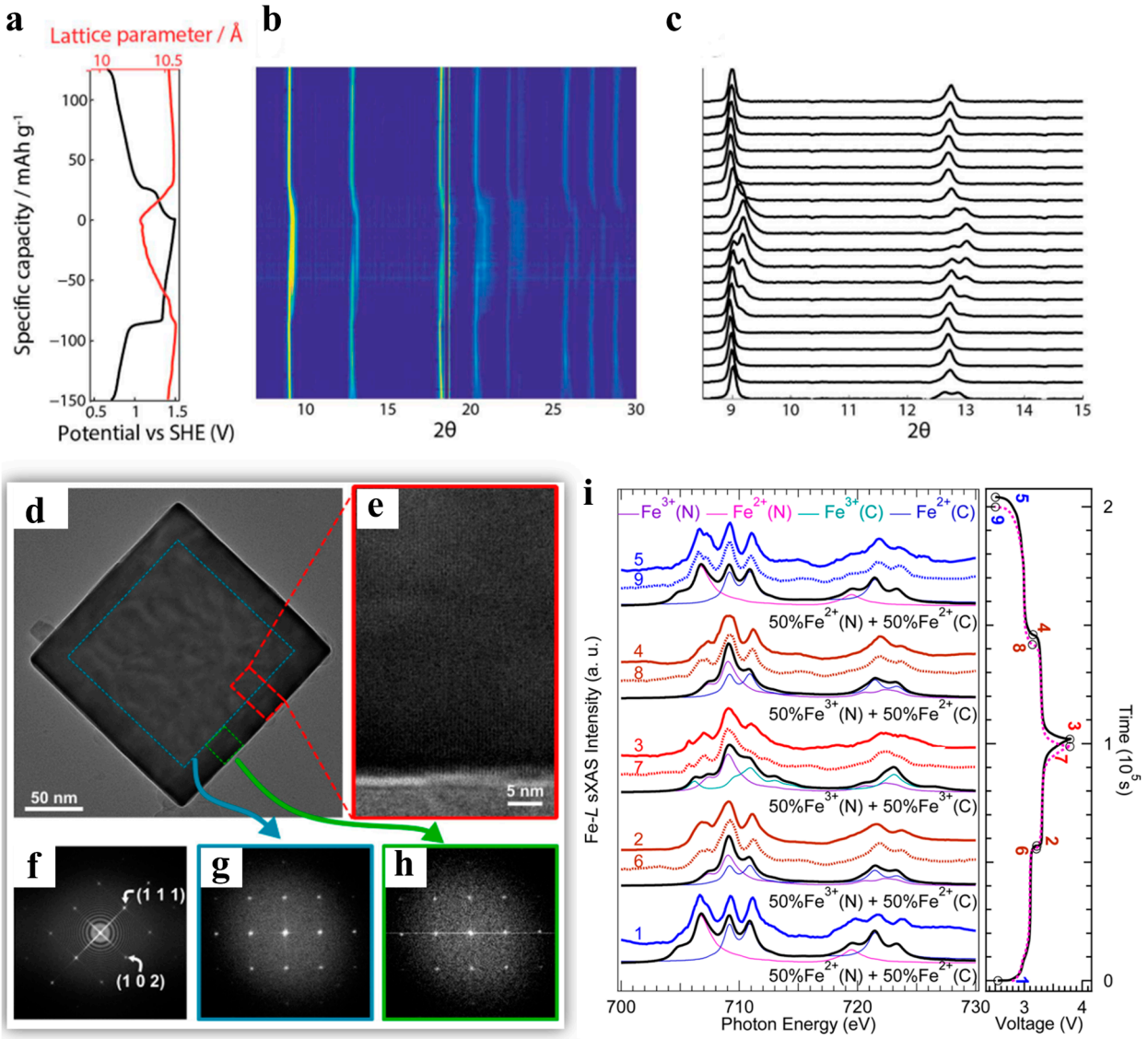


**Figure 3.** In situ synchrotron X-ray diffraction. (**a**) Galvanostatic charge–discharge curves at a 1C rate (black curve) and the cubic and rhombohedral lattice parameters (depending on the phase) (red curve)

of MnHCFe as a function of the state of charge. (**b**) Waterfall plots of the in situ synchrotron XRD measured at different charge states. The stripe around 18° is a result of the gap between adjacent X-ray detectors. The *y*-axis (specific capacity) is shared with panel (**a**). Higher peak intensities correspond to a brighter yellow color. This plot highlights trends in changing lattice parameter and phase transitions upon cycling. (**c**) Individual diffractograms at selected states of charge that accentuate changes in peak intensities and width [85]. (**d**) Cryo-HRTEM image of a MnNiPB-4xcit crystal; the blue dotted line marks the border between the MnPB and NiPB phases. (**e**) Close-up image of the border region in red, (**f**) FFT of the entire particle, (**g**) FFT of the core (MnPB phase) only, and (**h**) FFT of the outer layer indicated by green dotted line (NiPB phase) only [87]. (**i**) Fe L-edge sXAS spectra (TEY) collected on a series of Prussian white cathode samples cycled to different electrochemical states. The simulated spectra are shown in black [88].

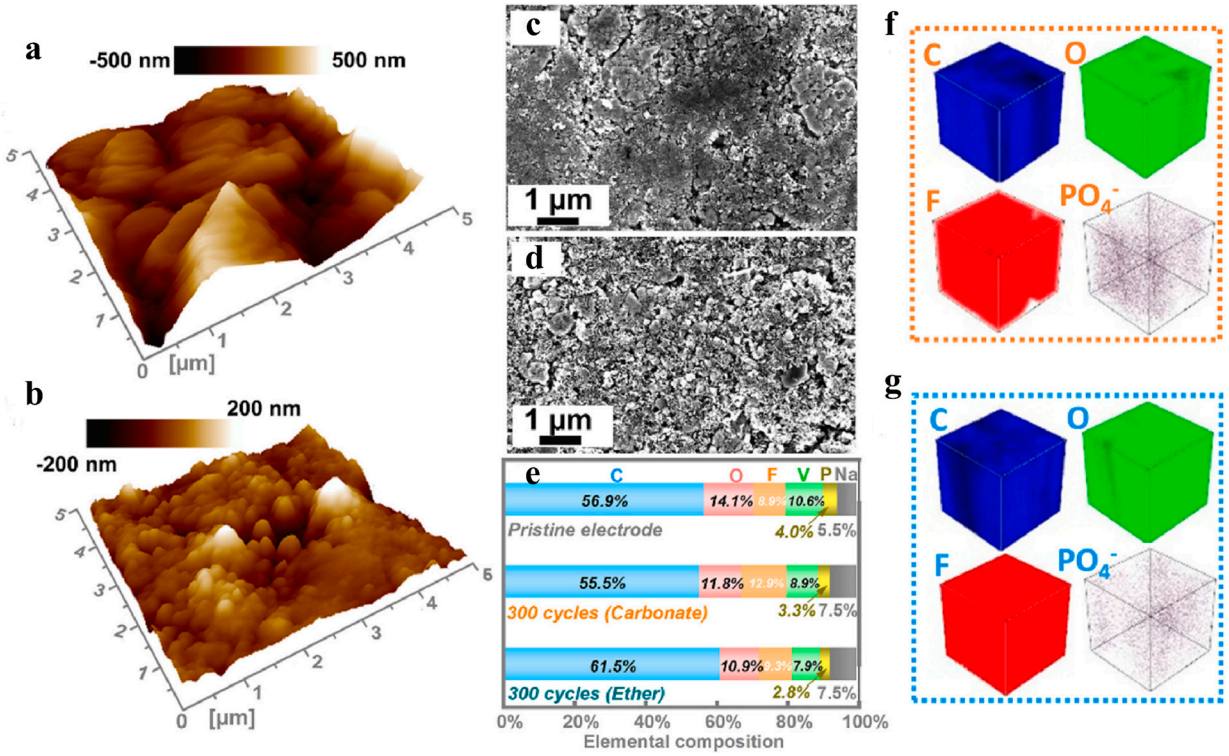


**Figure 4.** Typical atomic force microscopy (AFM) images of $Na_3V_2(PO_4)_3$ electrodes after 50 cycles in (**a**) 1 M $NaPF_6$-PC/FEC electrolyte and (**b**) 1 M $NaPF_6$-DGME electrolyte, respectively. Typical scanning electron microscopy (SEM) images of $Na_3V_2(PO_4)_2F_3$ morphologies after 300 cycles in (**c**) 1 M $NaPF_6$-PC/FEC electrolyte and (**d**) 1 M $NaPF_6$-DGME electrolyte, and (**e**) the corresponding elemental composition according to energy-dispersive spectroscopy (EDS) mapping. Three-dimensional view of $C^-$, $O^-$, $F^-$, and $PO_4^{5-}$ species according to time-of-flight secondary-ion mass spectrometry (TOF-SIMS) analysis with sputtering from top to bottom in the selected area of $Na_3V_2(PO_4)_2F_3$ electrodes after 50 cycles in 1 M $NaPF_6$-PC/FEC electrolyte (**f**) and 1 M $NaPF_6$-DGME electrolyte (**g**), respectively [93].

While advanced characterization may pose challenges in real-time analysis and encounter issues related to sample preparation, the complexity of the experimental design, and data interpretation, their significance remains indisputable. Advanced characterization techniques on cathodes serve pivotal roles in the following:

1. Unraveling the redox mechanism within SIBs to shape the choice of chemistry tailored for diverse applications;
2. Assessing the interface stability and validating the cell designs for the development of long-life-span SIBs;

3. Understanding the failure mechanism across different materials, and offering insights for future material engineering pathways (Figure 5).

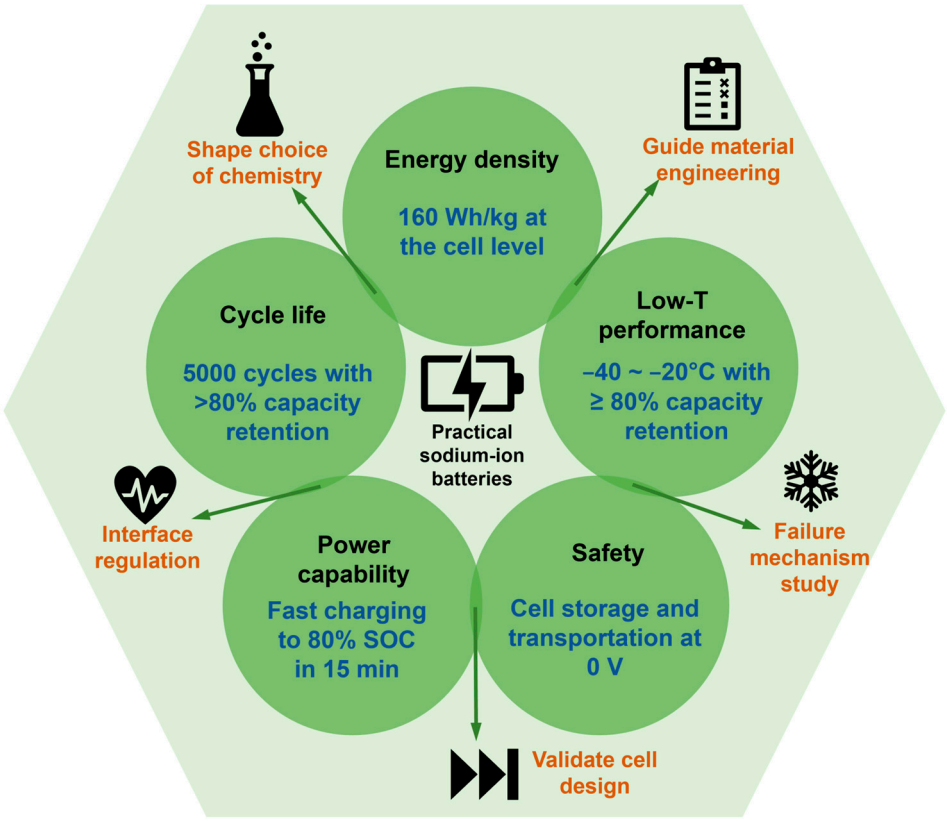


**Figure 5.** Role of advanced characterizations towards practical SIBs.

Without these comprehensive in-depth studies, rapid technology commercialization would be unattainable.

## 4. Conclusions

SIBs have gained attention for their utilization of electrode materials that do not contain expensive or ethically problematic elements such as cobalt; instead, they employ readily available transition metal elements, which make the technology a promising solution towards using batteries beyond lithium-ion batteries. Academia and industry have both witnessed a resurgence in SIB development in recent years despite a period of reduced research in the field following the successful commercialization of LIBs. Notably, recent breakthroughs, such as the release of CATL's first-generation SIB, have demonstrated compelling energy densities, extended cycle lifetimes, and rapid charging capabilities, effectively positioning SIBs as formidable contenders for electric vehicle applications. Furthermore, the proliferation of other companies, including Tiamat Energy, Faradion Ltd., Natron Energy, and HiNa Battery Technology, underscores the industry's commitment to achieving comparable performance with lithium-ion-based counterparts. However, it is important to recognize that despite significant progress being made, several scientific challenges remain unresolved. The need for advanced characterization techniques, ranging from elemental analyses to advanced spectroscopic and microscopic investigations, has become increasingly essential in the pursuit of optimizing SIB performance and understanding failure mechanisms. This concerted effort in advanced characterization, coupled with ongoing endeavors in battery manufacturing and testing, holds the key to expediting the successful commercialization of SIBs for widespread electric vehicle adoption and various other applications. This review emphasizes the critical role of advanced characterization

findings in guiding the optimization and commercial deployment of SIBs, highlighting their potential to meet current parameters and fulfill commercial objectives effectively.

**Funding:** This research at Oak Ridge National Laboratory, managed by UT-Battelle, LLC, for the U.S. Department of Energy (DOE) under contract number DE-AC05-00OR22725, was sponsored by Energy Storage Research, Office of Electricity (OE) and by the Office of Energy Efficiency and Renewable Energy (EERE) Vehicle Technologies Office (VTO).

**Data Availability Statement:** The data presented in this study are available on request from the corresponding author.

**Conflicts of Interest:** The author declares no conflict of interest.

## References

1. Whittingham, M.S.; Huggins, R.A. Measurement of sodium ion transport in beta alumina using reversible solid electrodes. *J. Chem. Phys.* **1971**, *54*, 414–416. [CrossRef]
2. Tarascon, J.; Hull, G. Sodium intercalation into the layer oxides $Na_xMo_2O_4$. *Solid State Ion.* **1986**, *22*, 85–96. [CrossRef]
3. Doeff, M.M.; Peng, M.Y.; Ma, Y.; De Jonghe, L. Orthorhombic $Na_xMnO_2$ as a cathode material for secondary sodium and lithium polymer batteries. *J. Electrochem. Soc.* **1994**, *141*, L145. [CrossRef]
4. Delmas, C.; Braconnier, J.-J.; Fouassier, C.; Hagenmuller, P. Electrochemical intercalation of sodium in $Na_xCoO_2$ bronzes. *Solid State Ion.* **1981**, *3*, 165–169. [CrossRef]
5. Delmas, C.; Cherkaoui, F.; Nadiri, A.; Hagenmuller, P. A nasicon-type phase as intercalation electrode: $NaTi_2(PO_4)_3$. *Mater. Res. Bull.* **1987**, *22*, 631–639. [CrossRef]
6. Kezuka, K.; Hatazawa, T.; Nakajima, K. The status of Sony Li-ion polymer battery. *J. Power Source* **2001**, *97*, 755–757. [CrossRef]
7. Buiel, E.; Dahn, J. Li-insertion in hard carbon anode materials for Li-ion batteries. *Electrochim. Acta* **1999**, *45*, 121–130. [CrossRef]
8. Buiel, E.; George, A.; Dahn, J. Model of micropore closure in hard carbon prepared from sucrose. *Carbon* **1999**, *37*, 1399–1407. [CrossRef]
9. Buiel, E.; Dahn, J. Reduction of the Irreversible Capacity in Hard-Carbon Anode Materials Prepared from Sucrose for Li-Ion Batteries. *J. Electrochem. Soc.* **1998**, *145*, 1977. [CrossRef]
10. Lu, Y.; Wang, L.; Cheng, J.; Goodenough, J.B. Prussian blue: A new framework of electrode materials for sodium batteries. *Chem. Commun.* **2012**, *48*, 6544–6546. [CrossRef]
11. Lee, H.; Kim, Y.-I.; Park, J.-K.; Choi, J.W. Sodium zinc hexacyanoferrate with a well-defined open framework as a positive electrode for sodium ion batteries. *Chem. Commun.* **2012**, *48*, 8416–8418. [CrossRef]
12. Wu, X.; Deng, W.; Qian, J.; Cao, Y.; Ai, X.; Yang, H. Single-crystal FeFe (CN) 6 nanoparticles: A high capacity and high rate cathode for Na-ion batteries. *J. Mater. Chem. A* **2013**, *1*, 10130–10134. [CrossRef]
13. Wessells, C.D.; Peddada, S.V.; Huggins, R.A.; Cui, Y. Nickel hexacyanoferrate nanoparticle electrodes for aqueous sodium and potassium ion batteries. *Nano Lett.* **2011**, *11*, 5421–5425. [CrossRef] [PubMed]
14. Baumann, M.; Häringer, M.; Schmidt, M.; Schneider, L.; Peters, J.F.; Bauer, W.; Binder, J.R.; Weil, M. Prospective Sustainability Screening of Sodium-Ion Battery Cathode Materials. *Adv. Energy Mater.* **2022**, *12*, 2202636. [CrossRef]
15. Available online: https://www.catl.com/en/news/685.html (accessed on 29 July 2021).
16. He, M.; Mejdoubi, A.E.; Chartouni, D.; Morcrette, M.; Troendle, P.; Castiglioni, R. High power NVPF/HC-based sodium-ion batteries. *J. Power Source* **2023**, *588*, 233741. [CrossRef]
17. Zhou, Q.; Li, Y.; Tang, F.; Li, K.; Rong, X.; Lu, Y.; Chen, L.; Hu, Y.-S. Thermal stability of high power 26650-type cylindrical Na-ion batteries. *Chin. Phys. Lett.* **2021**, *38*, 076501. [CrossRef]
18. Available online: https://news.metal.com/newscontent/101860656/natrium-energy-signed-a-contract-of-80000-mt-of-sodium-ion-battery-cathode-material-project-further-accelerating-the-industrialisation/ (accessed on 14 June 2022).
19. Lu, J.; Wu, T.; Amine, K. State-of-the-art characterization techniques for advanced lithium-ion batteries. *Nat. Energy* **2017**, *2*, 17011. [CrossRef]
20. Shen, Q.; Liu, Y.; Jiao, L.; Qu, X.; Chen, J. Current state-of-the-art characterization techniques for probing the layered oxide cathode materials of sodium-ion batteries. *Energy Storage Mater.* **2021**, *35*, 400–430. [CrossRef]
21. Wang, L.; Liu, T.; Wu, T.; Lu, J. Exploring new battery knowledge by advanced characterizing technologies. In *Exploration*; Wiley Online Library: Hoboken, NJ, USA, 2021; p. 20210130.
22. Li, Q.; Liu, Z.; Zheng, F.; Liu, R.; Lee, J.; Xu, G.L.; Zhong, G.; Hou, X.; Fu, R.; Chen, Z. Identifying the structural evolution of the sodium ion battery $Na_2FePO_4F$ cathode. *Angew. Chem.* **2018**, *130*, 12094–12099. [CrossRef]
23. Wang, W.; Gang, Y.; Hu, Z.; Yan, Z.; Li, W.; Li, Y.; Gu, Q.-F.; Wang, Z.; Chou, S.-L.; Liu, H.-K. Reversible structural evolution of sodium-rich rhombohedral Prussian blue for sodium-ion batteries. *Nat. Commun.* **2020**, *11*, 980. [CrossRef]
24. Zhu, Y.F.; Xiao, Y.; Hua, W.B.; Indris, S.; Dou, S.X.; Guo, Y.G.; Chou, S.L. Manipulating layered P2@ P3 integrated spinel structure evolution for high-performance sodium-ion batteries. *Angew. Chem. Int. Ed.* **2020**, *59*, 9299–9304. [CrossRef]
25. Jiang, Y.; Yu, S.; Wang, B.; Li, Y.; Sun, W.; Lu, Y.; Yan, M.; Song, B.; Dou, S. Prussian blue@ C composite as an ultrahigh-rate and long-life sodium-ion battery cathode. *Adv. Funct. Mater.* **2016**, *26*, 5315–5321. [CrossRef]

26. Song, T.; Yao, W.; Kiadkhunthod, P.; Zheng, Y.; Wu, N.; Zhou, X.; Tunmee, S.; Sattayaporn, S.; Tang, Y. A low-cost and environmentally friendly mixed polyanionic cathode for sodium-ion storage. *Angew. Chem.* **2020**, *132*, 750–755. [CrossRef]
27. Cao, X.; Li, H.; Qiao, Y.; Li, X.; Jia, M.; Cabana, J.; Zhou, H. Stabilizing reversible oxygen redox chemistry in layered oxides for sodium-ion batteries. *Adv. Energy Mater.* **2020**, *10*, 1903785. [CrossRef]
28. Wang, P.-F.; Xiao, Y.; Piao, N.; Wang, Q.-C.; Ji, X.; Jin, T.; Guo, Y.-J.; Liu, S.; Deng, T.; Cui, C. Both cationic and anionic redox chemistry in a P2-type sodium layered oxide. *Nano Energy* **2020**, *69*, 104474. [CrossRef]
29. Zhao, Q.; Wang, W.; Li, Y.-t.; Wu, N.; Guo, Y.-d.; Cheng, W.-j.; Sun, W.-w.; Li, J.-z.; Zhou, A.-j. Ion-exchange surface modification enhances cycling stability and kinetics of sodium manganese hexacyanoferrate cathode in sodium-ion batteries. *Electrochim. Acta* **2021**, *390*, 138842. [CrossRef]
30. Yang, L.; Liu, Q.; Wan, M.; Peng, J.; Luo, Y.; Zhang, H.; Ren, J.; Xue, L.; Zhang, W. Surface passivation of $Na_xFe[Fe(CN)_6]$ cathode to improve its electrochemical kinetics and stability in sodium-ion batteries. *J. Power Source* **2020**, *448*, 227421. [CrossRef]
31. Li, J.; Hu, H.; Wang, J.; Xiao, Y. Surface chemistry engineering of layered oxide cathodes for sodium-ion batteries. *Carbon Neutralization* **2022**, *1*, 96–116. [CrossRef]
32. Nelson, P.A.; Ahmed, S.; Gallagher, K.G.; Dees, D.W. *Modeling the Performance and Cost of Lithium-Ion Batteries for Electric-Drive Vehicles*; Argonne National Lab (ANL): Argonne, IL, USA, 2019.
33. Li, M.Y.; Du, Z.J.; Khaleel, M.A.; Belharouak, I. Materials and engineering endeavors towards practical sodium-ion batteries. *Energy Storage Mater.* **2020**, *25*, 520–536. [CrossRef]
34. Vaalma, C.; Buchholz, D.; Weil, M.; Passerini, S. A cost and resource analysis of sodium-ion batteries. *Nat. Rev. Mater.* **2018**, *3*, 18013. [CrossRef]
35. Muruganantham, R.; Chiu, Y.-T.; Yang, C.-C.; Wang, C.-W.; Liu, W.-R. An efficient evaluation of F-doped polyanion cathode materials with long cycle life for Na-ion batteries applications. *Sci. Rep.* **2017**, *7*, 14808. [CrossRef]
36. Yang, L.; Li, X.; Liu, J.; Xiong, S.; Ma, X.; Liu, P.; Bai, J.; Xu, W.; Tang, Y.; Hu, Y.-Y. Lithium-doping stabilized high-performance $P2–Na_{0.66}Li_{0.18}Fe_{0.12}Mn_{0.7}O_2$ cathode for sodium ion batteries. *J. Am. Chem. Soc.* **2019**, *141*, 6680–6689. [CrossRef]
37. Wang, J.; Mi, C.; Nie, P.; Dong, S.; Tang, S.; Zhang, X. Sodium-rich iron hexacyanoferrate with nickel doping as a high performance cathode for aqueous sodium ion batteries. *J. Electroanal. Chem.* **2018**, *818*, 10–18. [CrossRef]
38. Lamb, J.; Manthiram, A. Surface-modified Na $(Ni_{0.3}Fe_{0.4}Mn_{0.3})O_2$ cathodes with enhanced cycle life and air stability for sodium-ion batteries. *ACS Appl. Energy Mater.* **2021**, *4*, 11735–11742. [CrossRef]
39. Chen, M.; Chen, L.; Hu, Z.; Liu, Q.; Zhang, B.; Hu, Y.; Gu, Q.; Wang, J.L.; Wang, L.Z.; Guo, X. Carbon-Coated $Na_{3.32}Fe_{2.34}(P_2O_7)_2$ Cathode Material for High-Rate and Long-Life Sodium-Ion Batteries. *Adv. Mater.* **2017**, *29*, 1605535. [CrossRef] [PubMed]
40. Zhang, Q.; Fu, L.; Luan, J.; Huang, X.; Tang, Y.; Xie, H.; Wang, H. Surface engineering induced core-shell Prussian blue@ polyaniline nanocubes as a high-rate and long-life sodium-ion battery cathode. *J. Power Source* **2018**, *395*, 305–313. [CrossRef]
41. Available online: https://natron.energy/product/ (accessed on 6 October 2023).
42. Li, Y.; Zhao, Y.; Feng, X.; Wang, X.; Shi, Q.; Wang, J.; Wang, J.; Zhang, J.; Hou, Y. A durable P2-type layered oxide cathode with superior low-temperature performance for sodium-ion batteries. *Sci. China -Mater.* **2022**, *65*, 328–336. [CrossRef]
43. You, Y.; Yao, H.R.; Xin, S.; Yin, Y.X.; Zuo, T.T.; Yang, C.P.; Guo, Y.G.; Cui, Y.; Wan, L.J.; Goodenough, J.B. Subzero-temperature cathode for a sodium-ion battery. *Adv. Mater.* **2016**, *28*, 7243–7248. [CrossRef]
44. Gu, Z.Y.; Guo, J.Z.; Sun, Z.H.; Zhao, X.X.; Wang, X.T.; Liang, H.J.; Zhao, B.; Li, W.H.; Pan, X.M.; Wu, X.L. Aliovalent-ion-induced lattice regulation based on charge balance theory: Advanced fluorophosphate cathode for sodium-ion full batteries. *Small* **2021**, *17*, 2102010. [CrossRef]
45. Available online: https://natron.energy/battery-safety/ (accessed on 28 September 2022).
46. Zhao, E.Y.; Wang, H.W.; Yin, W.; He, L.H.; Ke, Y.B.; Wang, F.W.; Zhao, J.K. Spatiotemporal-scale neutron studies on lithium-ion batteries and beyond. *Appl. Phys. Lett.* **2022**, *121*, 110501. [CrossRef]
47. Beck, F.R.; Cheng, Y.; Bi, Z.; Feygenson, M.; Bridges, C.A.; Moorhead-Rosenberg, Z.; Manthiram, A.; Goodenough, J.B.; Paranthaman, M.P.; Manivannan, A. Neutron diffraction and electrochemical studies of $Na_{0.79}CoO_2$ and $Na_{0.79}Co_{0.7}Mn_{0.3}O_2$ cathodes for sodium-ion batteries. *J. Electrochem. Soc.* **2014**, *161*, A961. [CrossRef]
48. Li, Z.-Y.; Ma, X.; Sun, K.; He, L.; Li, Y.; Chen, D. $Na_{2/3}Li_{1/9}$ $[Ni_{2/9}Li_{1/9}Mn_{2/3}]O_2$: A high-performance solid-solution reaction layered oxide cathode material for sodium-ion batteries. *ACS Appl. Energy Mater.* **2021**, *5*, 1126–1135. [CrossRef]
49. Nielsen, I.; Dzodan, D.; Ojwang, D.O.; Henry, P.F.; Ulander, A.; Ek, G.; Häggström, L.; Ericsson, T.; Boström, H.; Brant, W. Water driven phase transitions in Prussian white cathode materials. *J. Phys. Energy* **2022**, *4*, 044012. [CrossRef]
50. Barpanda, P.; Avdeev, M.; Ling, C.D.; Lu, J.; Yamada, A. Magnetic structure and properties of the $Na_2CoP_2O7$ pyrophosphate cathode for sodium-ion batteries: A supersuperexchange-driven non-collinear antiferromagnet. *Inorg. Chem.* **2013**, *52*, 395–401. [CrossRef]
51. Ma, T.; Xu, G.-L.; Zeng, X.; Li, Y.; Ren, Y.; Sun, C.; Heald, S.M.; Jorne, J.; Amine, K.; Chen, Z. Solid state synthesis of layered sodium manganese oxide for sodium-ion battery by in-situ high energy X-ray diffraction and X-ray absorption near edge spectroscopy. *J. Power Source* **2017**, *341*, 114–121. [CrossRef]
52. Bai, X.; Sathiya, M.; Mendoza-Sánchez, B.; Iadecola, A.; Vergnet, J.; Dedryvère, R.; Saubanère, M.; Abakumov, A.M.; Rozier, P.; Tarascon, J.M. Anionic redox activity in a newly Zn-doped sodium layered oxide P2-$Na_{2/3}Mn_{1-y}Zn_yO_2$ ($0 < y < 0.23$). *Adv. Energy Mater.* **2018**, *8*, 1802379.

53. Tripathi, A.; Rudola, A.; Gajjela, S.R.; Xi, S.; Balaya, P. Developing an $O_3$ type layered oxide cathode and its application in 18650 commercial type Na-ion batteries. *J. Mater. Chem. A* **2019**, *7*, 25944–25960. [CrossRef]
54. Sottmann, J.; Bernal, F.L.; Yusenko, K.V.; Herrmann, M.; Emerich, H.; Wragg, D.S.; Margadonna, S. In operando synchrotron XRD/XAS investigation of sodium insertion into the Prussian Blue Analogue Cathode material $Na_{1.32}Mn[Fe(CN)_6]_{0.83}\cdot z\ H_2O$. *Electrochim. Acta* **2016**, *200*, 305–313. [CrossRef]
55. Xiao, B.; Liu, X.; Chen, X.; Lee, G.H.; Song, M.; Yang, X.; Omenya, F.; Reed, D.M.; Sprenkle, V.; Ren, Y. Uncommon behavior of Li doping suppresses oxygen redox in P2-type manganese-rich sodium cathodes. *Adv. Mater.* **2021**, *33*, 2107141. [CrossRef]
56. Hakim, C.; Sabi, N.; Ma, L.A.; Dahbi, M.; Brandell, D.; Edström, K.; Duda, L.C.; Saadoune, I.; Younesi, R. Understanding the redox process upon electrochemical cycling of the P2-$Na_{0.78}Co_{1/2}Mn_{1/3}Ni_{1/6}O_2$ electrode material for sodium-ion batteries. *Commun. Chem.* **2020**, *3*, 9. [CrossRef] [PubMed]
57. House, R.A.; Maitra, U.; Pérez-Osorio, M.A.; Lozano, J.G.; Jin, L.; Somerville, J.W.; Duda, L.C.; Nag, A.; Walters, A.; Zhou, K.-J. Superstructure control of first-cycle voltage hysteresis in oxygen-redox cathodes. *Nature* **2020**, *577*, 502–508. [CrossRef]
58. Lombardo, T.; Walther, F.; Kern, C.; Moryson, Y.; Weintraut, T.; Henss, A.; Rohnke, M. ToF-SIMS in battery research: Advantages, limitations, and best practices. *J. Vac. Sci. Technol. A* **2023**, *41*, 053207. [CrossRef]
59. Ma, X.H.; Chen, H.L.; Ceder, G. Electrochemical Properties of Monoclinic $NaMnO_2$. *J. Electrochem. Soc.* **2011**, *158*, A1307–A1312. [CrossRef]
60. Yabuuchi, N.; Yoshida, H.; Komaba, S. Crystal Structures and Electrode Performance of Alpha-$NaFeO_2$ for Rechargeable Sodium Batteries. *Electrochemistry* **2012**, *80*, 716–719. [CrossRef]
61. Zhu, Y.H.; Nie, W.Y.; Chen, P.P.; Zhou, Y.F.; Xu, Y. Li-doping stabilized P2-$Li_{0.2}Na_{1.0}Mn_{0.8}O_2$ sodium ion cathode with oxygen redox activity. *Int. J. Energ. Res.* **2020**, *44*, 3253–3259. [CrossRef]
62. Velikokhatnyi, O.I.; Choi, D.; Kumta, P.N. Effect of boron on the stability of monoclinic $NaMnO_2$: Theoretical and experimental studies. *Mater. Sci. Eng. B-Solid* **2006**, *128*, 115–124. [CrossRef]
63. Clément, R.J.; Billaud, J.; Armstrong, A.R.; Singh, G.; Rojo, T.; Bruce, P.G.; Grey, C.P. Structurally stable Mg-doped P2-$Na_{2/3}Mn_{1-y}Mg_yO_2$ sodium-ion battery cathodes with high rate performance: Insights from electrochemical, NMR and diffraction studies. *Energy Environ. Sci.* **2016**, *9*, 3240–3251. [CrossRef]
64. Nayak, D.; Jha, P.K.; Ghosh, S.; Adyam, V. Aluminium substituted β–type $NaMn_{1-x}Al_xO_2$: A stable and enhanced electrochemical kinetic sodium-ion battery cathode. *J. Power Source* **2019**, *438*, 227025. [CrossRef]
65. Sato, T.; Yoshikawa, K.; Zhao, W.; Kobayashi, T.; Rajendra, H.B.; Yonemura, M.; Yabuuchi, N. Efficient stabilization of Na storage reversibility by Ti integration into O′ 3-type $NaMnO_2$. *Energy Mater. Adv.* **2021**, *2021*, 9857563.
66. Choi, J.U.; Park, Y.J.; Jo, J.H.; Kuo, L.Y.; Kaghazchi, P.; Myung, S.T. Unraveling the Role of Earth-Abundant Fe in the Suppression of Jahn-Teller Distortion of P′2-Type $Na_{2/3}MnO_2$: Experimental and Theoretical Studies. *Acs Appl. Mater. Interfaces* **2018**, *10*, 40978–40984. [CrossRef]
67. Hemalatha, K.; Jayakumar, M.; Prakash, A. Influence of the manganese and cobalt content on the electrochemical performance of P2-$Na_{0.67}Mn_xCo_{1-x}O_2$ cathodes for sodium-ion batteries. *Dalton Trans.* **2018**, *47*, 1223–1232. [CrossRef] [PubMed]
68. Kalapsazova, M.; Stoyanova, R.; Zhecheva, E.; Tyuliev, G.; Nihtianova, D. Sodium deficient nickel–manganese oxides as intercalation electrodes in lithium ion batteries. *J. Mater. Chem. A* **2014**, *2*, 19383–19395. [CrossRef]
69. Ling, Y.X.; Zhou, J.; Guo, S.; Fu, H.W.; Zhou, Y.F.; Fang, G.Z.; Wang, L.B.; Lu, B.A.; Cao, X.X.; Liang, S.Q. Copper-Stabilized P′2-Type Layered Manganese Oxide Cathodes for High-Performance Sodium-Ion Batteries. *Acs Appl. Mater. Interfaces* **2021**, *13*, 58665–58673. [CrossRef]
70. Wu, X.H.; Xu, G.L.; Zhong, G.M.; Gong, Z.L.; McDonald, M.J.; Zheng, S.Y.; Fu, R.Q.; Chen, Z.H.; Amine, K.; Yang, Y. Insights into the Effects of Zinc Doping on Structural Phase Transition of P2-Type Sodium Nickel Manganese Oxide Cathodes for High-Energy Sodium Ion Batteries. *Acs Appl. Mater. Interfaces* **2016**, *8*, 22227–22237. [CrossRef] [PubMed]
71. Song, B.H.; Hu, E.Y.; Liu, J.; Zhang, Y.M.; Yang, X.Q.; Nanda, J.; Huq, A.; Page, K. A novel P3-type $Na_{2/3}Mg_{1/3}Mn_{2/3}O_2$ as high capacity sodium-ion cathode using reversible oxygen redox. *J. Mater. Chem. A* **2019**, *7*, 1491–1498. [CrossRef]
72. Rong, X.H.; Liu, J.; Hu, E.Y.; Liu, Y.J.; Wang, Y.; Wu, J.P.; Yu, X.Q.; Page, K.; Hu, Y.S.; Yang, W.L.; et al. Structure-Induced Reversible Anionic Redox Activity in Na Layered Oxide Cathode. *Joule* **2018**, *2*, 125–140. [CrossRef]
73. Jin, Y.; Xu, Y.B.; Le, P.M.L.; Vo, T.D.; Zhou, Q.; Qi, X.G.; Engelhard, M.H.; Matthews, B.E.; Jia, H.; Nie, Z.M.; et al. Highly Reversible Sodium Ion Batteries Enabled by Stable Electrolyte-Electrode Interphases. *Acs. Energy Lett.* **2020**, *5*, 3212–3220. [CrossRef]
74. Wang, H.; Liao, X.-Z.; Yang, Y.; Yan, X.; He, Y.-S.; Ma, Z.-F. Large-scale synthesis of $NaNi_{1/3}Fe_{1/3}Mn_{1/3}O_2$ as high performance cathode materials for sodium ion batteries. *J. Electrochem. Soc.* **2016**, *163*, A565. [CrossRef]
75. Xie, Y.; Gao, H.; Harder, R.; Li, L.; Gim, J.; Che, H.; Wang, H.; Ren, Y.; Zhang, X.; Li, L. Revealing the Structural Evolution and Phase Transformation of $O_3$-Type $NaNi_{1/3}Fe_{1/3}Mn_{1/3}O_2$ Cathode Material on Sintering and Cycling Processes. *ACS Appl. Energy Mater.* **2020**, *3*, 6107–6114. [CrossRef]
76. Xie, Y.; Xu, G.-L.; Che, H.; Wang, H.; Yang, K.; Yang, X.; Guo, F.; Ren, Y.; Chen, Z.; Amine, K. Probing thermal and chemical stability of $Na_xNi_{1/3}Fe_{1/3}Mn_{1/3}O_2$ Cathode material toward safe sodium-ion batteries. *Chem. Mater.* **2018**, *30*, 4909–4918. [CrossRef]

77. Yao, H.R.; Wang, P.F.; Gong, Y.; Zhang, J.N.; Yu, X.Q.; Gu, L.; OuYang, C.Y.; Yin, Y.X.; Hu, E.Y.; Yang, X.Q.; et al. Designing Air-Stable O3-Type Cathode Materials by Combined Structure Modulation for Na-Ion Batteries. *J. Am. Chem. Soc.* **2017**, *139*, 8440–8443. [CrossRef] [PubMed]
78. Qin, M.; Ren, W.; Jiang, R.; Li, Q.; Yao, X.; Wang, S.; You, Y.; Mai, L. Highly crystallized Prussian blue with enhanced kinetics for highly efficient sodium storage. *ACS Appl. Mater. Interfaces* **2021**, *13*, 3999–4007. [CrossRef]
79. He, S.; Zhao, J.; Rong, X.; Xu, C.; Zhang, Q.; Shen, X.; Qi, X.; Li, Y.; Li, X.; Niu, Y. Solvent-free mechanochemical synthesis of Na-rich Prussian white cathodes for high-performance Na-ion batteries. *Chem. Eng. J.* **2022**, *428*, 131083. [CrossRef]
80. You, Y.; Wu, X.-L.; Yin, Y.-X.; Guo, Y.-G. High-quality Prussian blue crystals as superior cathode materials for room-temperature sodium-ion batteries. *Energy Environ. Sci.* **2014**, *7*, 1643–1647. [CrossRef]
81. Wang, W.; Gang, Y.; Peng, J.; Hu, Z.; Yan, Z.; Lai, W.; Zhu, Y.; Appadoo, D.; Ye, M.; Cao, Y. Effect of eliminating water in prussian blue cathode for sodium-ion batteries. *Adv. Funct. Mater.* **2022**, *32*, 2111727. [CrossRef]
82. Fadzil, S.S.M.; Woo, H.; Azzahari, A.; Winie, T.; Kufian, M. Sodium-rich prussian blue analogue coated by poly(3,4-ethylenedioxythiophene) polystyrene sulfonate as superior cathode for sodium-ion batteries. *Mater. Today Chem.* **2023**, *30*, 101540. [CrossRef]
83. Adak, S.; Hartl, M.; Daemen, L.; Fohtung, E.; Nakotte, H. Study of oxidation states of the transition metals in a series of Prussian blue analogs using X-ray absorption near edge structure (XANES) spectroscopy. *J. Electron Spectrosc. Relat. Phenom.* **2017**, *214*, 8–19. [CrossRef]
84. Xie, B.; Zuo, P.; Wang, L.; Wang, J.; Huo, H.; He, M.; Shu, J.; Li, H.; Lou, S.; Yin, G. Achieving long-life Prussian blue analogue cathode for Na-ion batteries via triple-cation lattice substitution and coordinated water capture. *Nano Energy* **2019**, *61*, 201–210. [CrossRef]
85. Pasta, M.; Wang, R.Y.; Ruffo, R.; Qiao, R.; Lee, H.-W.; Shyam, B.; Guo, M.; Wang, Y.; Wray, L.A.; Yang, W. Manganese–cobalt hexacyanoferrate cathodes for sodium-ion batteries. *J. Mater. Chem. A* **2016**, *4*, 4211–4223. [CrossRef]
86. You, Y.; Wu, X.L.; Yin, Y.X.; Guo, Y.G. A zero-strain insertion cathode material of nickel ferricyanide for sodium-ion batteries. *J. Mater. Chem. A* **2013**, *1*, 14061–14065. [CrossRef]
87. Gebert, F.; Cortie, D.L.; Bouwer, J.C.; Wang, W.; Yan, Z.; Dou, S.X.; Chou, S.L. Epitaxial Nickel Ferrocyanide Stabilizes Jahn–Teller Distortions of Manganese Ferrocyanide for Sodium-Ion Batteries. *Angew. Chem.* **2021**, *133*, 18667–18674. [CrossRef]
88. Wang, L.; Song, J.; Qiao, R.M.; Wray, L.A.; Hossain, M.A.; Chuang, Y.D.; Yang, W.L.; Lu, Y.H.; Evans, D.; Lee, J.J.; et al. Rhombohedral Prussian White as Cathode for Rechargeable Sodium-Ion Batteries. *J. Am. Chem. Soc.* **2015**, *137*, 2548–2554. [CrossRef] [PubMed]
89. Panin, R.V.; Drozhzhin, O.A.; Fedotov, S.S.; Khasanova, N.R.; Antipov, E.V. NASICON-type $NaMo_2(PO_4)_3$: Electrochemical activity of the $Mo^{+4}$ polyanion compound in Na-cell. *Electrochim. Acta* **2018**, *289*, 168–174. [CrossRef]
90. Hadouchi, M.; Yaqoob, N.; Kaghazchi, P.; Tang, M.; Liu, J.; Sang, P.; Fu, Y.; Huang, Y.; Ma, J. Fast sodium intercalation in $Na_{3.41}£_{0.59}FeV(PO_4)_3$: A novel sodium-deficient NASICON cathode for sodium-ion batteries. *Energy Storage Mater.* **2021**, *35*, 192–202. [CrossRef]
91. Li, S.; Guo, J.; Ye, Z.; Zhao, X.; Wu, S.; Mi, J.-X.; Wang, C.-Z.; Gong, Z.; McDonald, M.J.; Zhu, Z. Zero-strain $Na_2FeSiO_4$ as novel cathode material for sodium-ion batteries. *ACS Appl. Mater. Interfaces* **2016**, *8*, 17233–17238. [CrossRef]
92. Wang, J.; Wang, Y.; Seo, D.H.; Shi, T.; Chen, S.; Tian, Y.; Kim, H.; Ceder, G. A high-energy NASICON-type cathode material for Na-ion batteries. *Adv. Energy Mater.* **2020**, *10*, 1903968. [CrossRef]
93. Qin, B.; Zarrabeitia, M.; Hoefling, A.; Jusys, Z.; Liu, X.; Tübke, J.; Behm, R.J.; Cui, G.; Varzi, A.; Passerini, S. A unique polymer-inorganic cathode-electrolyte-interphase (CEI) boosts high-performance $Na_3V_2(PO_4)_2F_3$ batteries in ether electrolytes. *J. Power Source* **2023**, *560*, 232630. [CrossRef]
94. Shin, K.H.; Park, S.K.; Nakhanivej, P.; Wang, Y.; Liu, P.; Bak, S.-M.; Choi, M.S.; Mitlin, D.; Park, H.S. Biomimetic composite architecture achieves ultrahigh rate capability and cycling life of sodium ion battery cathodes. *Appl. Phys. Rev.* **2020**, *7*, 041410. [CrossRef]
95. Chen, Y.; Xu, Y.; Sun, X.; Zhang, B.; He, S.; Li, L.; Wang, C. Preventing structural degradation from $Na_3V_2(PO_4)_3$ to $V_2(PO_4)_3$: F-doped $Na_3V_2(PO_4)_3$/C cathode composite with stable lifetime for sodium ion batteries. *J. Power Source* **2018**, *378*, 423–432. [CrossRef]
96. Chen, Y.; Xu, Y.; Sun, X.; Zhang, B.; He, S.; Wang, C. F-doping and V-defect synergetic effects on $Na_3V_2(PO_4)_3$/C composite: A promising cathode with high ionic conductivity for sodium ion batteries. *J. Power Source* **2018**, *397*, 307–317. [CrossRef]
97. Broux, T.; Bamine, T.; Simonelli, L.; Stievano, L.; Fauth, F.; Ménétrier, M.; Carlier, D.; Masquelier, C.; Croguennec, L. VIV disproportionation upon sodium extraction from $Na_3V_2(PO_4)_2F_3$ observed by operando X-ray absorption spectroscopy and solid-state NMR. *J. Phys. Chem. C* **2017**, *121*, 4103–4111. [CrossRef]
98. Iarchuk, A.R.; Sheptyakov, D.V.; Abakumov, A.M. Hydrothermal Microwave-Assisted Synthesis of $Na_{3+x}V_{2-y}Mn_y(PO_4)_2F_3$ Solid Solutions as Potential Positive Electrodes for Na-Ion Batteries. *Acs Appl. Energy Mater.* **2021**, *4*, 5007–5014. [CrossRef]
99. Gover, R.; Bryan, A.; Burns, P.; Barker, J. The electrochemical insertion properties of sodium vanadium fluorophosphate, $Na_3V_2(PO_4)_2F_3$. *Solid State Ion.* **2006**, *177*, 1495–1500. [CrossRef]

100. Liu, Y.M.; Wu, Z.G.; Indris, O.; Hua, W.B.; Casati, N.P.M.; Tayal, A.; Darma, M.S.D.; Wang, G.K.; Liu, Y.X.; Wu, C.J.; et al. The structural origin of enhanced stability of $Na_{3.32}Fe_{2.11}Ca_{0.23}(P_2O_7)_2$ cathode for Na-ion batteries. *Nano Energy* **2021**, *79*, 105417. [CrossRef]
101. Oyama, G.; Pecher, O.; Griffith, K.J.; Nishimura, S.-I.; Pigliapochi, R.; Grey, C.P.; Yamada, A. Sodium intercalation mechanism of 3.8 V class alluaudite sodium iron sulfate. *Chem. Mater.* **2016**, *28*, 5321–5328. [CrossRef]